International Journal of Bifurcation and Chaos

BIFURCATION DIAGRAMS AND GENERALIZED BIFURCATION DIAGRAMS FOR A ROTATIONAL MODEL OF AN OBLATE SATELLITE

MARIUSZ TARNOPOLSKI
Astronomical Observatory, Jagiellonian University, ul. Orla 171
Krakow, 30-244, Poland
mariusz.tarnopolski@uj.edu.pl

Received (to be inserted by publisher)

This paper presents bifurcation and generalized bifurcation diagrams for a rotational model of an oblate satellite. Special attention is paid to parameter values describing one of Saturn's moons, Hyperion. For various oblateness the largest Lyapunov Characteristic Exponent (LCE) is plotted. The largest LCE in the initial condition as well as in the mixed parameter-initial condition space exhibits a fractal structure, for which the fractal dimension was calculated. It results from the bifurcation diagrams of which most of the parameter values for preselected initial conditions lead to chaotic rotation. The First Recurrence Time (FRT) diagram provides an explanation of the birth of chaos and the existence of quasi-periodic windows occuring in the bifurcation diagrams.

Keywords: Hyperion, Bifurcation Diagrams, Generalized Bifurcation Diagrams, Lyapunov Characteristic Exponents.

1. Introduction

In many cases in the Solar System the assumption that planets and their satellites are particle-like is sufficient, e.g. in modelling many body motions or investigation of orbital resonances. Yet if the asphericity of a body is taken into account in many situations this may allow the encounter of measureable effects and explanation of observational occurences, e.g. the 3:2 spin-orbit resonance of Mercury [Goldreich & Peale, 1966]. Particularly, the rotational state of a nonspherical oblate satellite is nontrivial. Rotational dynamics is governed by the oblateness parameter, also called the ellipticity, $\omega^2 = 3(B-A)/C$, where $A < B < C$ are principal moments of inertia and C is the moment about the shortest physical axis. It is natural to assume that the spin axis is aligned with the axis of the largest moment of inertia and perpendicular to the orbit plane [Wisdom, 1987]. The tidal evolution of most known planets and satellites ensures trapping in the synchronous rotation. This indeed is true because of the small ellipticity for almost all moons within the Solar System[1]. Every a synchronously trapped satellite in its past had a period of time when its rotation was chaotic. Hyperion's high oblateness ($\omega^2 = 0.79$), however, has not allowed him to leave the chaotic zone, making it the largest known highly aspherical celestial body remaining in an exotic rotational state.

[1]Phobos is an exception as its oblateness is almost the same as Hyperion's, but it has small eccentricity, $e = 0.015$, and its evolution was significantly influenced by tidal friction due to its low orbit.

Wisdom *et al.* [1984] first studied the rotation of Hyperion in a comprehensive approach, including the research of attitude stability and tidal evolution. The Poincaré surface of section proved that the phase space is dominated by a chaotic zone. The largest LCE is positive and implies chaotic motion. The attitude instabillity was confirmed in a wide range of ratios A/C and B/C in the chaotic zone as well as in the resonance islands.

Small ellipticities are treatable by averaging or perturbing methods [Goldreich & Peale, 1966; Celletti, A. & Chierchia, L., 2000], although the growth of ω^2 wipes out low-order resonant islands leaving a vast chaotic zone, which definitely can not be explored in the means of the perturbation theory [Flynn, A. & Saha, P., 2005]. Numerical calculations containing dynamical systems' methods and standard tools of the theory of chaos are required.

Bifurcation diagrams (BDs) give a more global insight into a class of rotational systems' dynamics. The well known BD for a logistic map displays the period-doubling route to chaos as the nonlinear parameter grows. The same mechanism can be observed in other physical systems, e.g. the damped pendulum with driving [Baker, G. & Gollub, J., 1996]. BDs are suitable for determining nonlinear parameter values at which the system's behavior switches from regular to chaotic and *vice versa* as well as for searching strictly periodic solutions of a given dynamical system. This approach, however, can only allow research over one parameter, while the others, if present, and the initial conditions (ICs), have to be fixed. Generalized BDs (GBDs), obtained by plotting the largest LCE on an IC surface or a mixed space, reveal a fractal structure and give complete information about bifurcation cascades [Manchein, C. & Beims, M., 2013]. If the oblateness is set as a free parameter one can investigate how does the change of its value affect the rotational dynamics of such a body. This kind of research is not yet to be found in any literature.

This paper is organized in the following manner. Sec. 2 introduces the model, parameters and numerical methods that have been used. In Sec. 3 BDs are presented, where the nonlinear parameter varied is the ellipticity. A comparison of predictions based on the BDs and the largest LCE plot is conducted. In Sec. 4 GBDs are used to explain the discrepancy between the respective methods of the previous section. The fractal character of the diagrams is emphasized. Sec. 5 gathers results of fractional dimension analysis of the GBDs. The box counting dimension and the correlation dimension are used to prove the fractality of the sets and provide their qualitative characteristic. Sec. 6 is devoted to the First Recurrence Time (FRT) analysis, which allows to explain the origin of chaotic and regular zones present on the BDs and GBDs. Concluding remarks are given in Sec. 7.

2. Model and Parameters

The model used is based on the following assumptions:

(a) the orbit of the satellite is Keplerian with the eccentricity e and the semi-major axis a,
(b) the satellite is considered to be a triaxial ellipsoid and its spin axis is perpendicular to the orbit plane,
(c) the spin axis is aligned with the shortest physical axis, i.e. the one corresponding to the largest principal moment of inertia,
(d) the following equation of motion can be derived using the double dumbbell model for the satellite's shape [Greiner, W., 2010].

The equation of motion is

$$\ddot{\theta} + \frac{\omega^2}{2r^3} \sin 2(\theta - f) = 0, \tag{1}$$

where r is the instantaneous radius, f — the true anomaly, $\theta - f$ is the angle between the longest physical axis and the direction to the planet, the dot denotes the time derivative and $\theta = \theta(t)$ is the dynamical variable fully describing the rotation, so the system has one degree of freedom. Units have been chosen so that the orbital period is equal to 2π and $a = 1$. Rewritting the equation in a standard dynamical system form gives:

$$\dot{\theta} = \varphi, \tag{2}$$

$$\dot{\varphi} = -\frac{\omega^2}{2r^3}\sin 2(\theta - f), \tag{3}$$

$$\dot{f} = \frac{(1 + e\cos f)^2}{(1 - e^2)^{3/2}}, \tag{4}$$

where Eq. (4) describes the time evolution of the true anomaly. The parameters that describe Hyperion are $\omega^2 = 0.79$ and $e = 0.1$. In all cases the IC for Eq. (4) is chosen to be $f(0) \equiv f_0 = 0$. ICs: $\theta(0) \equiv \theta_0$ and $\dot{\theta}(0) \equiv \dot{\theta}_0$ are varied. In this article, the computer algebra system Mathematica is employed. Calculation of LCEs has been performed using an algorithm described in [Sandri, M., 1996], based on the method formulated by Benettin *et al.* [1980a,b]. The correlation sum is calculated using a parallel Python program.

3. Bifurcation Diagrams with Largest LCE Plot

For a good understanding of the nature of bifurcation diagrams it is necessary to start with an analysis of the structure of the phase space.

3.1. *Poincaré section*

The phase space, as indicated from Eq. (2)–(4), is three-dimensional, though the f direction of the phase flow is time-like: mathematically, $f(t)$ is a monotonically increasing function, so for all t it is possible to rewrite Eq. (1) using f as the independent variable [Wisdom *et al.*, 1984]. The solution then is valid for all values of f, which geometrically is an angle with a periodically repeating value (if taken modulo 2π). Thus the general features of the phase space are clearly visible on a two dimensional Poincaré surface of section presented in Fig. 1 (with parameters suitable for Hyperion). For simplicity the stroboscopic $\theta \times \dot{\theta}$ space will be called the phase space. Also, the IC space will be widely used. The chaotic zone's size is of the order of

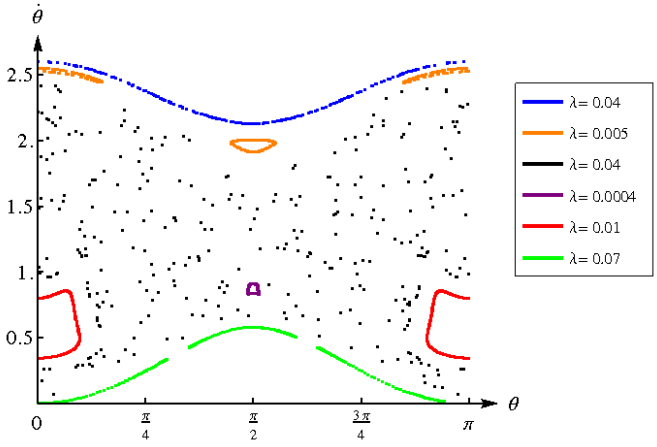

Fig. 1. Poincaré surface of section for two librational and three rotational quasiperiodic orbits and one chaotic orbit. The box displays the largest LCE for each of these orbits.

the phase space's size. Regular orbits may be categorized into two classes: periodic, which consist a finite amount of points, and quasiperiodic, whose plot on the Poincaré section are analytic lines. The latter can be divided into librational and rotational ones. Librational periodic orbits surround resonant islands. All regular orbits have a smaller span in the $\dot{\theta}$ direction than the chaotic ones, so plotting the $\dot{\theta}$ values versus the nonlinear parameter is a suitable way of obtaining bifurcation diagrams.

3.2. *Bifurcation diagrams*

The equation of motion has two free parameters: eccentricity e and oblateness ω^2. In order to obtain BDs the eccentricity is fixed and for each value of ω^2 from an interval from 0 to 1, taken with a step equal to

0.005, the values of $\dot{\theta}$ in a stroboscopic view are plotted. Simultaneously, the largest LCE is calculated for ICs $\theta_0 = 0$ and $\dot{\theta}_0 = 1$. The result is shown in Fig. 2 for a couple of e values.

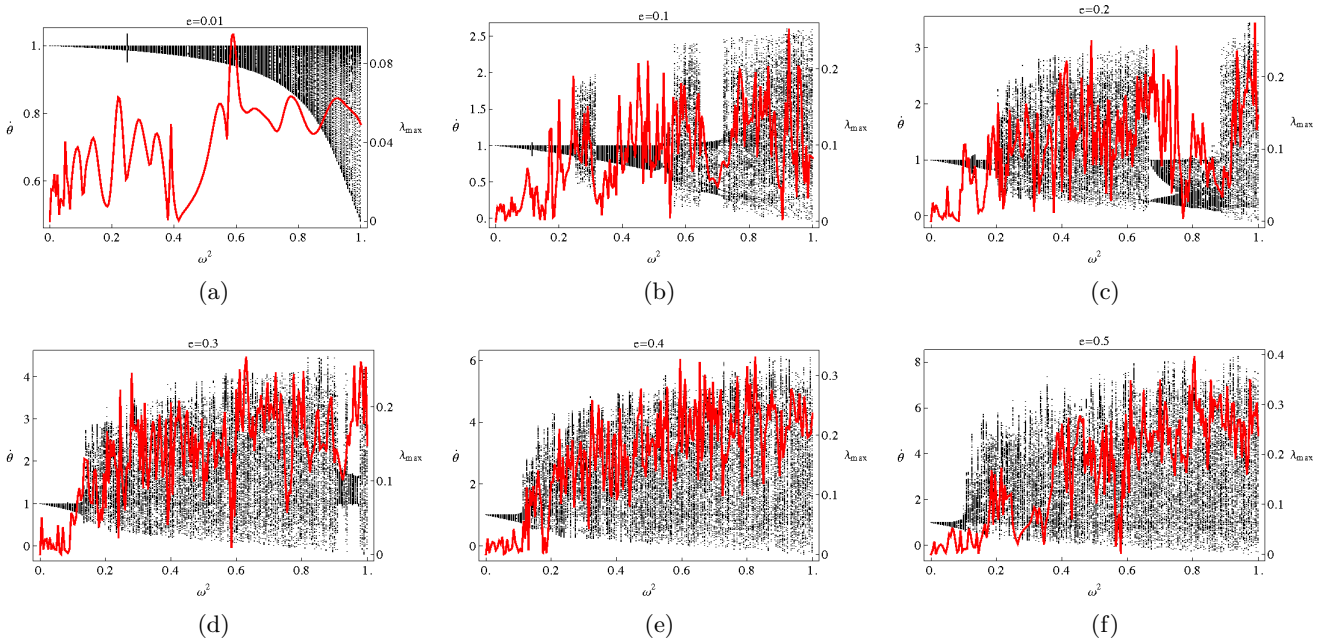

Fig. 2. BDs and largest LCE plots for eccentricities up to $e = 0.5$. Plots for $e > 0.5$ exhibit roughly the same behavior as shown in figures (e) and (f) with increasing value of the $\dot{\theta}$ span.

For given ICs, all orbits obtained for $e = 0.01$ are quasiperiodic, surrounding the $p = 1/2$ resonant island. For Hyperion's eccentricity the result is nontrivial. Knowing the structure of the phase space one can identify three significant regions of chaotic motion: first for oblateness from about 0.25 to 0.32, second from 0.56 to 0.65 and the third from 0.72 to 1.0. At 0.52 a switch from one type of quasiperiodic motion (the red orbit from Fig. 1) to another (a subtype of the orange one) is observed. The motion at 0.70 is periodic with a presence of higher harmonics. For Hyperion's oblateness the motion is chaotic. BD for $e = 0.2$ is slightly different. The quasiperiodic region up to 0.18 surrounds a chaotic area at 0.12. The center of the BD contains a vast chaotic zone, followed again by quasiperiodic orbits and periodic windows at 0.83. High ω^2 provide chaotic rotation. For $e = 0.3$, the BD is dominated by chaotic behavior, with unexpected quasiperiodic windows for ω^2 from 0.91 to 0.98 with a thin chaotic region at 0.94. For higher eccentricities, quasiperiodic orbits occur for small values of oblateness and BDs are dominated by a wide chaotic zone.

A magnification for $e = 0.2$ is shown in Fig. 3. Several strictly periodic orbits are found within the magnified region, starting from the two-period one at $\omega^2 = 0.19$ through others, consisting of higher harmonics. Two branches, arising from the two-period orbit, merge into a chaotic zone for $\omega^2 \approx 0.198$. The route to chaos seems to proceed via some period multiplying process, although not via the well known period-doubling. Periodic solutions are common and frequently spaced in the quasiperiodic region.

The LCE plot is more ambiguous. Not only chaotic, but also quasiperiodic orbits have assigned positive largest LCE. As indicated in [Manchein, C. & Beims, M., 2013] this is due to the convergent properties of the iterative procedure of obtaining LCEs. Different ICs give distinct convergence rates, however, as the procedure has to be stopped after a finite number of iterations, the LCEs are not given enough time to converge to zero, what should happen if the infinite limit in the definition of the LCE is conducted[2]. As pointed out for a discrete map, relatively small LCEs correspond to irrational tori surrounding periodic

[2]The zero valued LCE, corresponding to the f direction in the phase space, is neglected here.

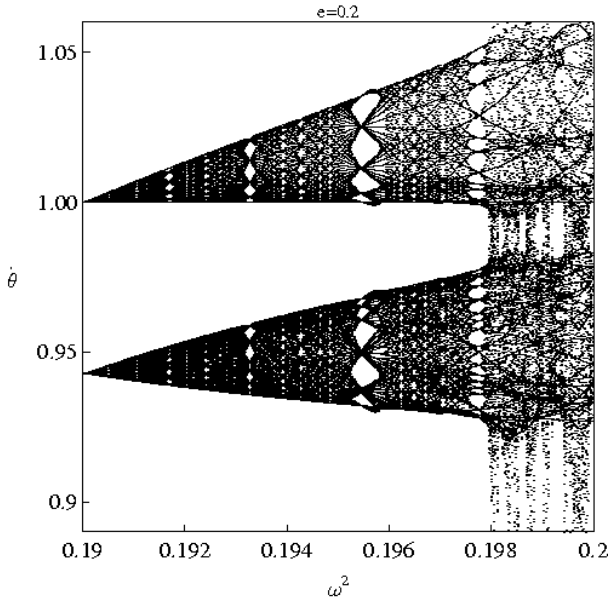

Fig. 3. Magnification of Fig. 2(c) with ω^2 step equal to $2.5 \cdot 10^{-5}$. The right side chaotic zone is a result of merging two regular branches who compete for stabilization of the orbit.

regions. Therefore chaotic solutions should be characterized by greater LCEs than the regular ones and having plotted the LCE dependence on the nonlinear parameter one should be able to distinguish between those two. Fig. 2(a) roughly confirms this conclusion — LCE values are relatively small (if LCEs for the chaotic zone is known). On the other hand, Fig. 1 contradicts this reasoning: the black, chaotic trajectory has a smaller LCE than a quasiperiodic green one. Taking into account Fig. 2(b)–2(f) one finds only slight qualitative resemblance to the BDs. Yet searching for a deeper interpretation of the LCE dependence on IC should be taken into account.

4. Generalized Bifurcation Diagrams

Fig. 4 presents the largest LCE on an IC space for parameter values appropriate for Hyperion. This diagram reveals approximately a similar structure as shown in Fig. 1. Calculating Poincaré surface of sections for some arbitrarily chosen ICs among the values displayed in Fig. 4 leads to a following corollary: green marked regions of the phase space correspond to ICs giving rise to regular trajectories and the red ones provide chaotic rotation. Moreover, the red area seems to posses a fractal structure, which is a nontrivial observation to be examined later on. A magnification of a part of the IC space, presented in Fig. 5, strongly supports the hypothesis about the fractality.

It is surprising that this diagram is not symmetric as Fig. 1 would indicate. This feature has been confirmed to appear for other values of e and ω^2, implying it is a genuine property of the system examined. A hint toward explanation of this phenomenon is suggested in [Manchein, C. & Beims, M., 2013]. Calculated LCEs are not the *real* ones, but are affected by the finiteness of the iterative procedure. This would suggest that the system (2)–(4) exhibits a slow, varying from point to point, convergence of the LCEs to its limit values. This, as well as the origin of the fractal structure, awaits for verification.

Having the above corollary stated, it is possible to analyze the structure of the mixed space $\omega^2 \times \dot{\theta}_0$ for $\theta_0 = 0$, presented in Fig. 6.

The mixed space also seems to have a fractal structure of the same type as suggested above, with "tongues" of high LCEs penetrating the regular motion areas and low LCE values creeping in the chaotic zone. It is justifiable to compare this result with Fig. 2(b), taking a section at $\dot{\theta}_0 = 1$: for small ω^2 the motion is regular, at about 0.25 the LCE rises and crosses the pass between two "red valued" protrusions of chaotic motion, hence a conjecture of turning to chaos is justified. Thereafter the motion returns to a regular state and eventually ends in a chaotic region starting at $\omega^2 \approx 0.6$. Although a significant decrease

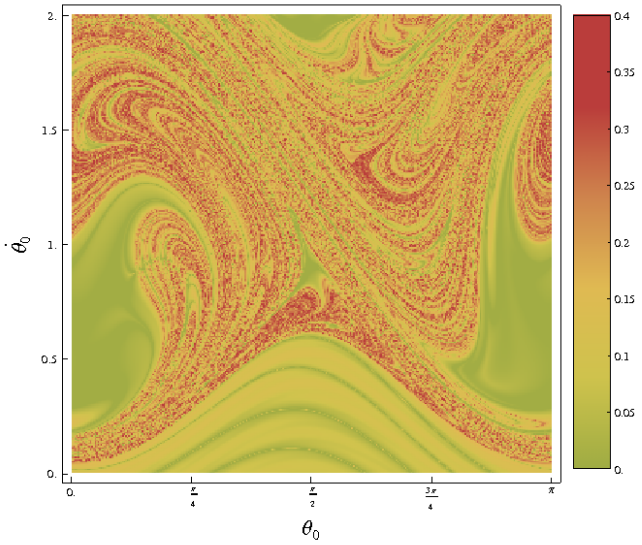

Fig. 4. Largest LCE plotted on an IC space with a grid of 300×300 points. Note the change in scale from Fig. 1.

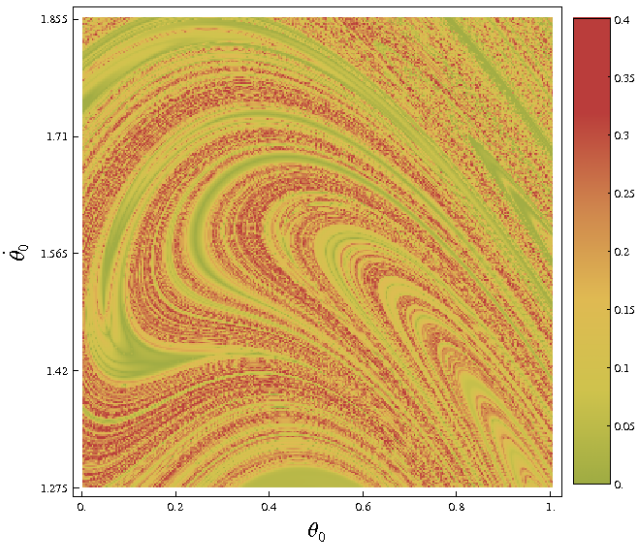

Fig. 5. Magnification of a part of the IC space with a grid of 300×300 points.

of the LCE in Fig. 2(b) is in good correlation with the bifurcation diagram, a magnification of the GBD (not shown herein) does not reveal a relatively thin regular region submerged in the chaotic zone.

In reference to the results mentioned above, an analogous diagram for $\theta_0 = \pi/2$ is generated and shown in Fig. 7. Diagrams in Fig. 4–7 all exhibit a fractal, i.e. self-similar, structure, which is examined in the next section.

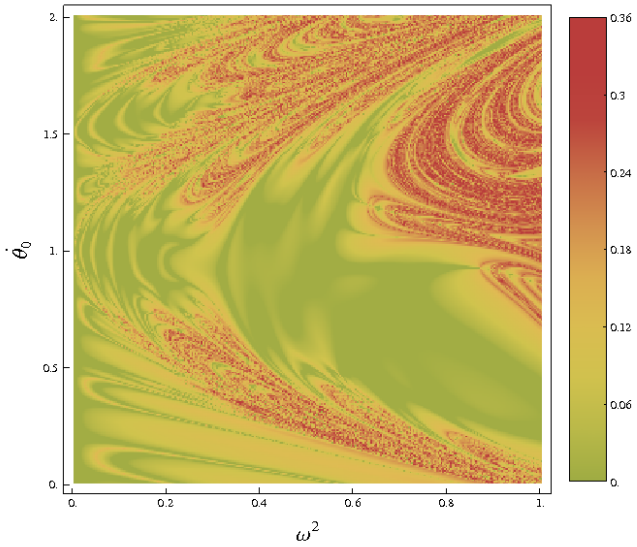

Fig. 6. Largest LCE plotted on a mixed space with a grid of 300×300 points for Hyperion's eccentricity $e = 0.1$ and $\theta_0 = 0$. The span of the LCE is near the one from Fig. 4.

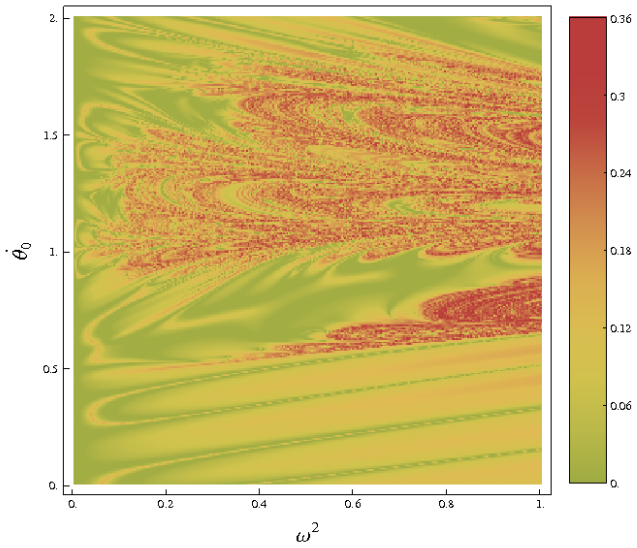

Fig. 7. Largest LCE plotted on a mixed space with a grid of 300×300 points for $\theta_0 = \pi/2$.

5. Fractal Analysis

The research is based on calculation of the fractal dimension of the structures formed by higher-valued LCEs on the IC and mixed space. To extract those structures, a following procedure is applied. For a given threshold τ all LCEs smaller than τ are removed from the diagram, while the remaining ones are assumed to form a spatial distribution on a two-dimensional surface. As a result of this operation diagrams from

Fig. 8–10 are obtained.

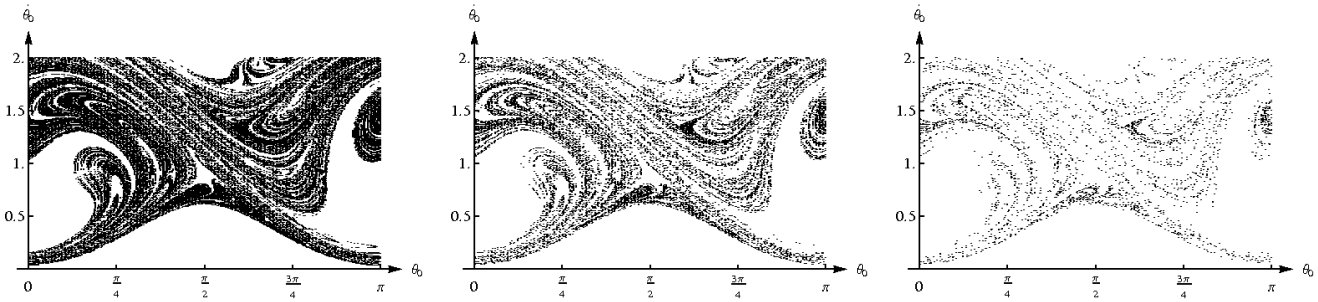

(a) (b) (c)

Fig. 8. (a)–(c) LCE diagrams obtained for thresholds $\tau = 0.1,\ 0.15$ and 0.2 respectively, for the IC space.

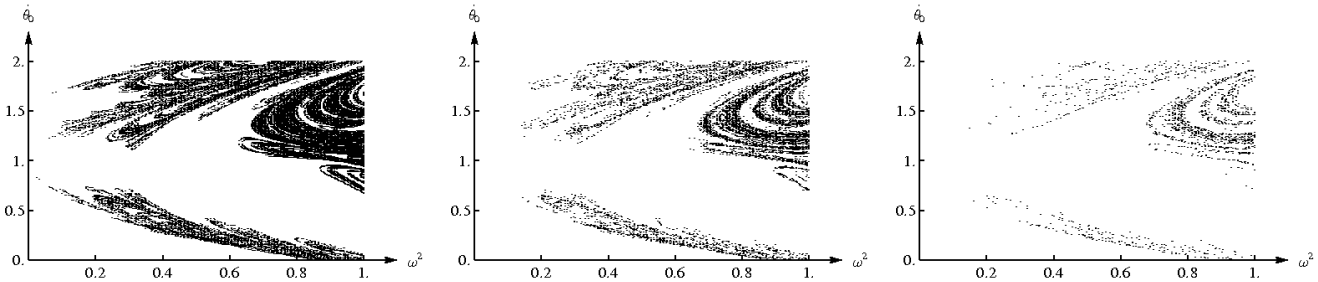

(a) (b) (c)

Fig. 9. (a)–(c) LCE diagrams obtained for thresholds $\tau = 0.1,\ 0.15$ and 0.2 respectively, for the mixed space and $\theta_0 = 0$.

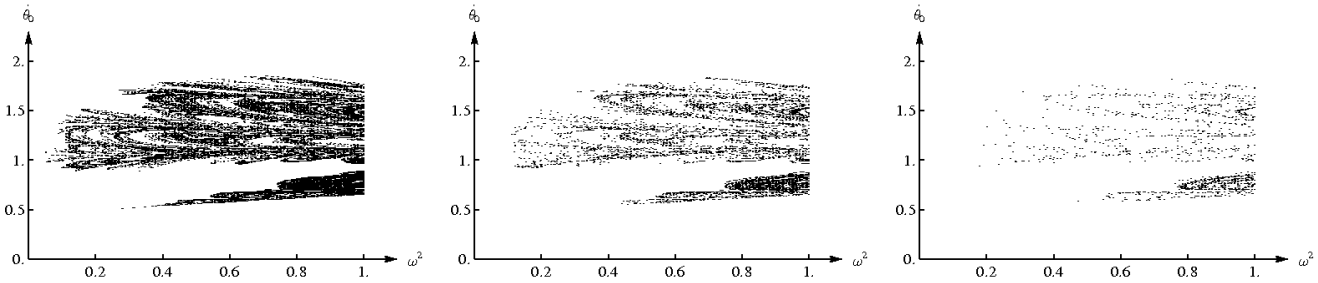

(a) (b) (c)

Fig. 10. (a)–(c) LCE diagrams obtained for thresholds $\tau = 0.1,\ 0.15$ and 0.2 respectively, for the mixed space and $\theta_0 = \pi/2$.

The fractal dimension (strictly speaking, the Hausdorff dimension) is estimated in two ways: through the box counting and the correlation dimension. The box counting dimension is defined as

$$d_C = \lim_{\varepsilon \to 0} \frac{\ln N(\varepsilon)}{\ln(1/\varepsilon)}, \tag{5}$$

where $N(\varepsilon)$ is the number of non-empty boxes (squares) of the size ε. The correlation dimension is

defined as[3]

$$d_G = \lim_{r\to 0} \frac{\ln C(r)}{\ln r}, \tag{6}$$

with the estimate for the correlation function $C(r)$ as

$$C(r) = \lim_{N\to\infty} \left[\frac{1}{N^2} \sum_{i=1}^{N} \sum_{j=i+1}^{N} H(r - ||x_i - x_j||) \right], \tag{7}$$

where the Heaviside step function H adds to $C(r)$ only points x_i in a distance smaller than r from x_j and *vice versa*. Both limits in Eq. (5) and (6) are attained by using small values of ε and r respectively and by fitting a straight line to the obtained dependencies. The fractal dimension is estimated as the slope of the linear regression. The results are gathered in Table 1.

Table 1. Fractal dimensions for fractals created from the largest LCE plots. Each threshold leads to distinct set of N points. The uncertainties here are standard deviations of the linear regressions' slopes. The actual uncertainties are larger because of the finiteness of sets, numerical errors and the arbitrary choice which part of the plot is linear.

	Threshold	N	Box counting dimension	Correlation dimension
IC space	0.1	34 234	1.64 ± 0.05	1.90 ± 0.01
	0.15	12 817	1.53 ± 0.05	1.82 ± 0.01
	0.2	3118	1.48 ± 0.04	1.73 ± 0.01
Mixed space with $\theta_0 = 0$	0.1	18 779	1.57 ± 0.03	1.84 ± 0.01
	0.15	6835	1.43 ± 0.03	1.77 ± 0.01
	0.2	1541	1.28 ± 0.01	1.69 ± 0.01
Mixed space with $\theta_0 = \pi/2$	0.1	15 720	1.55 ± 0.05	1.83 ± 0.01
	0.15	5409	1.50 ± 0.04	1.77 ± 0.01
	0.2	1241	1.35 ± 0.03	1.69 ± 0.01

The box counting dimension varies with the threshold, which is a natural consequence of different amounts and spacings between points forming researched sets. The fewer points, the bigger is the minimum box size ε, what leads to a less reliable estimate for d_C. Increasing the number of points forming examined sets leads to a higher value of d_C, but the more points, the smaller the minimal box can be, so the box counting dimension approaches the limit from Eq. (5). Unfortunately, achieving this goal means calculating the LCE distribution in the IC or mixed space with a higher grid than used herein, what due to at least quadratically increasing numerical cost is very memory consuming. Therefore the correlation dimension is a better estimate for the Hausdorff dimension because it takes into account the distribution of points. Obtained d_G values are greater than the d_C ones and, as stated above, give a more reliable estimation on the fractal dimension. However, they also depend on the number of points[4]. The minimal r from Eq. (6) reaches the minimal distance between points in each set.

[3]The index G is in honor of Grassberger [Grassberger, P. & Procaccia, I., 1983].

[4]For large enough N the fractal dimension should achieve a limit which, within the desired precision, does not change with further increase of N. This has been checked, for refference, for the Duffing attractor [Tarnopolski, M., 2013].

6. First Recurrence Time

The method of obtaining and general features of the First Recurrence Time (FRT) diagrams were described in detail in [Manchein, C. & Beims, M., 2013]. In this paper, the distance $d(t)$ between the trajectory and the IC is an Euclidean distance:

$$d(t) = \sqrt{\left(\theta(t) - \theta_0\right)^2 + \left(\dot{\theta}(t) - \dot{\theta}_0\right)^2}. \tag{8}$$

Integrations were performed over an interval $t \in (0, 10^4)$; if, after leaving the neighbourhood of the IC (defined as a circle of a radius $d_0 = 10^{-2}$), the trajectory returned to it within the integration time, the FRT was recorded as the time spent outside the neighbourhood. Otherwise, a value of 10^4 was recorded.

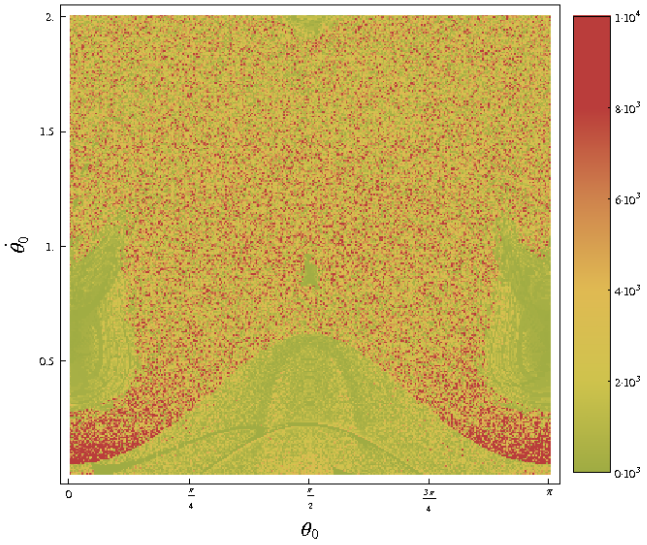

Fig. 11. The FRT diagram on the IC space with a grid of 300×300 points, with clearly visible resonant islands in the chaotic sea. Note the change in vertical scale from Fig. 1.

For the IC space the obtained diagram in Fig. 11 has the same structure as in Fig. 1. This was to be expected because of the transitivity of the flow and local properties of the trajectory for each IC.

The FRT diagram for the mixed-space is shown in Fig. 12. This is in fine correspondence with the LCE plot in Fig. 6. Moreover, the hypothesis that the passing between two chaotic protrusions is the cause of the first chaotic region in the bifurcation diagram in Fig. 2(b) is now well justified: those protrusions in fact connect, forcing the trajectory to become chaotic. Also, the onset of the quasi-periodic window on the right side of Fig. 2(b) can be predicted on the basis of the FRT diagram, which posseses in general the same features as the LCE diagram, but provides more accurate predictions on the character of a given trajectory's behavior. This may be due to the convergence properties of the LCE.

7. Conclusions

This article presented bifurcation diagrams for a simplified rotational model of an oblate satellite on a Keplerian orbit. Classical BDs lead to a conclusion that for many values of the eccentricity e and oblateness ω^2 the rotation exhibits chaotic behavior. The largest LCE plot approximately supports this finding, although the quantitative results do not give reliable information about the motion's character. In the mixed space, the GBDs, based on the LCE calculation, provide an explanation of the onset of some

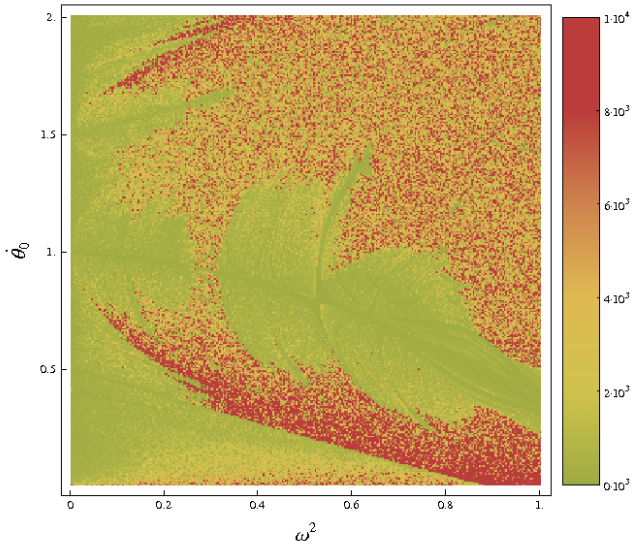

Fig. 12. The FRT diagram on a mixed space with a grid of 300×300 points and $\theta_0 = 0$. The leaf-like structure in the center exhibits soft bifurcations surrounded by a strong chaotic sea and enclosed by connecting protrusions on the left.

particular chaotic and regular zones due to a global view of the mixed space. Also, GBDs manifest a self-similar, i.e. fractal, structure. This has been verified by estimating the Hausdorff dimension in two ways: by the box counting and correlation dimensions. The obtained fractional dimension supports this suggestion, however the actual value varies with the number of points N forming the researched sets. Eventually, the FRT diagram gives a wide overlook of features and interferences of the mixed space's parts, resulting in a reliable explanation of the origin of particular chaotic and regular regions. Due to — as is supposed — poor convergence of LCEs for the investigated dynamical system, the FRT method seems to be a more decent candidate for the GBD in this case.

The above described research is sufficient for other Solar System bodies, i.e. planetoids, which often have irregular shape. Further studies can result in obtaining useful information concerning asteroids' behavior and artificial satellites' missions aiming at the exploration of the Solar System's small bodies.

Acknowledgments

The author is grateful to Slawomir Chrobak for the Python program that allowed to calculate the correlation dimension.

References

Baker, G. & Gollub, J. [1996] "Chaotic Dynamics: An Introduction", 2nd Ed. (Cambridge University Press).

Benettin, G., Galgani, A., Giorgilli, A. & Strelcyn, J. [1980] "Lyapunov characteristic exponents for smooth dynamical systems and for Hamiltonian systems; a method for computing all of them: Part 1. Theory", *Meccanica* **15**, 9–20.

Benettin, G., Galgani, A., Giorgilli, A. & Strelcyn, J. [1980] "Lyapunov characteristic exponents for smooth dynamical systems and for Hamiltonian systems; a method for computing all of them: Part 2. Numerical application", *Meccanica* **15**, 21–30.

Celletti, A. & Chierchia, L. [2000] "Hamiltonian stability of spin-orbit resonances in celestial mechanics", *Celest. Mech. Dyn. Astron.* **76**, 229–240.

Flynn, A. & Saha, P. [2005] "Second order perturbation theory for spin-orbit resonances", *The Astron. J.* **130**, 295–307.

Goldreich, P. & Peale, S. [1966] "Spin-Orbit Coupling in the Solar System", *The Astron. J.* **71**, 425–438.

Grassberger, P. & Procaccia, I. [1983] "Measuring the strangeness of strange attractors", *Physica D* **9**, 189–208.

Greiner, W. [2010] "Classical Mechanics. Systems of Particles and Hamiltonian Dynamics", (Springer-Verlag Berlin Heidelberg), Chapter 27, pp. 544–547.

Manchein, C. & Beims, M. [2013] "Conservative Generalized Bifurcation Diagrams", *Phys. Rev. A* **377**, 789–793.

Sandri, M. [1996] "Numerical Calculation of Lyapunov Exponents", *The Mathematica Journal* **6**, 78–84.

Tarnopolski, M. [2013] "On the fractal dimension of the Duffing attractor", arXiv:1305.6708 [nlin.CD].

Wisdom, J., Peale, S. & Mignard, F. [1984] "The Chaotic Rotation of Hyperion", *Icarus* **58**, 137–152.

Wisdom, J. [1987] "Chaotic behaviour in the Solar System", *Proc. R. Soc. Lond. A* **413**, 109–129.